

The Charged FENE-P Dumbbell model: explaining the rheology of dilute polyelectrolyte solutions

Dmitry Shogin^{1†}, and Per Amund Amundsen²

¹Department of Energy Resources, University of Stavanger, Norway

²Department of Mathematics and Physics, University of Stavanger, Norway

(Received xx; revised xx; accepted xx)

A robust model of dilute polyelectrolyte solutions is constructed based on kinetic theory arguments. The polyelectrolyte molecules are modelled by finitely elongated non-linear elastic dumbbells with beads carrying identical effective charges. The electric interaction between the beads is described in a simplified way through an electrostatic Coulomb force. With two pre-averaging approximations, the constitutive equations of the fluid model are formulated in closed form; and its rheological properties in steady and transient shear and elongational flows are investigated by analytical and simple numerical means. It is found that despite its simplicity, the model shows an excellent qualitative agreement with the results obtained by advanced numerical simulations of polyelectrolyte solutions and predicts most of the experimentally observed dynamical features of such fluids.

Declaration of interests. None.

1. Introduction

Polymeric liquids – liquids containing extremely long molecules – are of great importance for modern engineering and biotechnological applications. On the contrast to liquids consisting of small molecules, polymeric liquids are non-Newtonian: they do not obey the laws of classical fluid mechanics and often behave strictly opposite to what one could expect from "ordinary" fluids (Bird *et al.* 1987*a*, ch. 2).

Some synthetic and biological polymers are polyelectrolytes: they dissociate in water and become electrically charged. The segments of polyelectrolyte molecules carry charges of identical sign: this leads to repulsive electric forces, acting between different parts of the molecular chain. Such forces make polyelectrolyte molecules more rigid and rod-like, and therefore mechanically different from their electrically neutral analogues, as described by de Gennes *et al.* (1976).

One of the specific features of polyelectrolytes is that their rheological properties are strongly sensitive to kind and amount of ions present in the solvent. When the charged segments of a polyelectrolyte molecule attract ions of the opposite sign – e.g. from a dissolved salt – the repulsive force acting between the segments decreases due to screening; hence, the polyelectrolyte molecules become more flexible. This, of course, strongly affects the rheological behaviour of the solution.

Two major fields where flows of polyelectrolyte solutions are important, are biotechnology (Spagnolie 2014; Maitz 2015) and enhanced oil recovery (Lake 1989; Wever *et al.* 2011). In both cases, transient flows in non-trivial geometries are involved. In addition,

† Email address for correspondence: Dmitry.Shogin@uis.no

the salinity of the solvent may vary, making the flows of polyelectrolytes more complicated compared to those of uncharged polymers.

To understand the dynamics of such flows – even qualitatively – it is necessary to use advanced tensor models based on microscopic physics to adequately describe the forces governing the fluid motion; and these models must take the polyelectrolyte nature of the polymer into account. At the same time, such models need to be simple enough in order to be practically applicable at industrial scales and satisfy the demands of applied technology. Dumbbell models (Bird *et al.* 1987*b*, ch. 13-14) are a relatively simple class of fluid models for polymer solutions, derived from microscopic kinetic theory. Each polymer molecule is thought of as composed of two identical spherical beads connected by a spring (elastic dumbbell) or simply a rigid rod (rigid dumbbell). The configuration of each dumbbell is completely specified by the connector vector, \mathbf{Q} , pointing from one bead to another. Then, the properties of the molecules are defined by the connector force law, $\mathbf{F}_c(\mathbf{Q})$. In particular, the Warner force law (Warner 1972) has been found physically relevant:

$$\mathbf{F}_c(\mathbf{Q}) = \frac{H\mathbf{Q}}{1 - (Q/Q_0)^2}. \quad (1.1)$$

This law describes a non-linear spring of finite extensibility: the extension of the spring cannot exceed Q_0 , and the spring is Hookean with stiffness H at small extensions. Finite extensibility proves to be a crucial property for understanding the flow of polymer solutions. The resulting macroscopic fluid model is known as the FENE (finitely elongated non-linear elastic) dumbbell model (Armstrong 1974*a,b*). A pre-averaging approximation (closure) made by Peterlin (1966) allows to formulate the constitutive equations in closed form, facilitating both analytical investigation and numerical simulations of the fluid model. This updated version of the model is now known as FENE-P (“P” for Peterlin) and is probably the best dumbbell model to date. It is, however, restricted to electrically neutral or weakly hydrolysed polymers.

The pioneering attempt of constructing a dumbbell model describing polyelectrolyte solutions is that of King & Eisenberg (1972), who considered a Hookean dumbbell model modified by the presence of effective charges, interacting through an electrostatic Coulomb force. Then, Dunlap & Leal (1984) constructed an analogous fluid model based on FENE dumbbells; however, they adopted conformation-dependent friction. No closed-form constitutive equation was derived; and numerical simulations revealed a hysteretic behaviour of viscosity and relative elongation with respect to flow strength. Ait-Kadi *et al.* (1988) extended this work and formulated a constitutive equation for the model of Dunlap & Leal (1984), using a conformation tensor approach. Since then, the focus has been kept on implementing advanced numerical methods and improving the modelling of the electric repulsion between the charged polyelectrolyte parts: Andrews *et al.* (1998) considered screened Coulombic interactions using Nonequilibrium Brownian Dynamics and Configuration-Biased Monte Carlo simulations of charged Fraenkel bead-spring-chains; Jiang & Chen (2001) studied the impact of taking electroviscous effects into account; and Zhou & Chen (2006) investigated numerically the role played by hydrodynamic interaction.

In the present research, we are aiming at developing an effective phenomenological fluid model, which can be used to understand the rheology of polyelectrolyte solutions and describe qualitatively their behaviour in complex flows. Such a model must encapsulate all the crucial features of polyelectrolytes: orientability, non-linearity, finite extensibility, and variable intrinsic rigidity of the molecules – and at the same time be as simple as possible without suffering from pathologies of early kinetic theory models. For these

reasons, we take the successful FENE-P dumbbell model as our starting point. Although screened Coulombic interactions (with Debye-Hückel approximation) are a proper way to describe the repulsion between charged parts of polyelectrolyte molecules, this would also lead to substantial mathematical complexity. Therefore, we adopt the concept of effective charges, reverting to a simple Coulomb force, as proposed by Dunlap & Leal (1984).

The paper is organised as follows. In section 2, the underlying assumptions of the new polymer fluid model are specified and the closed-form constitutive equations are derived. Then, the constitutive equations are used to obtain the material functions predicted by the model; the results for steady and transient flows are presented in sections 3 and 4, respectively. The results are discussed in section 5; and conclusions are presented in section 6.

Throughout the paper, SI units are used. Scalars (such as density ρ , temperature T and shear rate $\dot{\gamma}$) are written with lightface italic font; vectors (such as force \mathbf{F} and velocity \mathbf{v}) – with boldface Latin; while second-order tensors (like rate-of-strain tensor $\dot{\boldsymbol{\gamma}}$ and stress tensor $\boldsymbol{\tau}$) – with boldface Greek. For the stress tensor, the sign convention of Bird *et al.* (1987a) is adopted.

2. The constitutive equations

The FENE dumbbell model is assumed applicable when the solution is sufficiently dilute, so that the polymer molecules interact with the molecules of the Newtonian solvent much stronger than with each other. The polymer-solvent interactions are typically described by an isotropic Stokes's law with conformation-independent coefficient ζ (Bird *et al.* 1987b, §13.1). It has been found that macroscopically the polymer contribution to the stress tensor of the solution depends on three parameters: the "ideal-gas" pressure nkT (where n is the number concentration of the dumbbells, k Boltzmann's constant, and T the thermodynamic temperature); the dimensionless non-linearity parameter $b = HQ_0^2/kT$; and a time constant, which we shall find it most convenient to define by:

$$\lambda = \lambda_Q = \frac{\zeta Q_0^2}{12kT}. \quad (2.1)$$

More commonly, $\lambda_H = 3\lambda_Q/b = \zeta/4H$ is used in literature. Our alternative choice of the time constant will be motivated below.

In order to describe qualitatively the electric repulsion between the charged sections of the polyelectrolyte chain, we assume the beads to carry identical *effective* charges q and the relative permittivity of the solvent to be ε . This modifies the connector force by an additional electrostatic Coulomb force, so that

$$\mathbf{F}_c = \frac{H\mathbf{Q}}{1 - (Q/Q_0)^2} - \frac{q^2}{4\pi\varepsilon_0\varepsilon} \frac{\mathbf{Q}}{Q^3}, \quad (2.2)$$

where ε_0 is the permittivity of vacuum.

Like for other dumbbell models, the stress tensor dilute polymer solutions can be split into a sum of solvent and polymer contributions:

$$\boldsymbol{\tau} = \boldsymbol{\tau}_s + \boldsymbol{\tau}_p. \quad (2.3)$$

Of these the latter, $\boldsymbol{\tau}_p$, can be written in two forms – the Kramers form and the Giesekus

form, respectively (Kramers 1944; Giesekus 1962); see also (Bird *et al.* 1987b, §13.3):

$$\boldsymbol{\tau}_p = -n\langle \mathbf{Q}\mathbf{F}_c \rangle + nkT\boldsymbol{\delta}, \quad (2.4)$$

$$\boldsymbol{\tau}_p = \frac{1}{4}n\zeta\langle \mathbf{Q}\mathbf{Q} \rangle_{(1)}. \quad (2.5)$$

Here the angular brackets denote the configuration-space average, see (Bird *et al.* 1987b, §13.1) for details; $\boldsymbol{\delta}$ is the unit tensor; while the subscript " $_{(1)}$ " stands for the upper-convected time derivative, introduced by Oldroyd (1950) to express the rate of change of tensor properties of a fluid element in a coordinate system deforming with the fluid.

Substituting the modified connector force (2.2) into the Kramers expression for the stress tensor (2.4), one gets:

$$\boldsymbol{\tau}_p = -nH \left\langle \frac{\mathbf{Q}\mathbf{Q}}{1 - (Q/Q_0)^2} \right\rangle + \frac{nq^2}{4\pi\epsilon_0\epsilon} \left\langle \frac{\mathbf{Q}\mathbf{Q}}{Q^3} \right\rangle + nkT\boldsymbol{\delta}. \quad (2.6)$$

In order to obtain the constitutive equation in closed form, this expression must be approximated by pre-averaging the first two terms. This is implemented as follows:

$$\left\langle \frac{\mathbf{Q}\mathbf{Q}}{1 - (Q/Q_0)^2} \right\rangle \approx \frac{\langle \mathbf{Q}\mathbf{Q} \rangle}{1 - \langle Q^2 \rangle / Q_0^2}, \quad (2.7)$$

$$\left\langle \frac{\mathbf{Q}\mathbf{Q}}{Q^3} \right\rangle \approx \frac{\langle \mathbf{Q}\mathbf{Q} \rangle}{\langle Q^2 \rangle^{3/2}}. \quad (2.8)$$

Approximation (2.7) is the Peterlin's closure, introduced when he established the FENE-P dumbbell polymer model (Peterlin 1966). The corresponding approximation for the Coulomb term, (2.8), is established by analogous arguments. We propose the abbreviation C-FENE-P for the present extended polymer model, where "C" stays for "charged".

In what follows, it will be convenient to introduce the dimensionless ratio

$$E = \frac{q^2}{(4\pi\epsilon_0\epsilon Q_0)kT} \quad (2.9)$$

between the characteristic potential energy of the electric repulsion and the thermal energy scale of the dumbbells. Alternatively, $E = z^2 l_B / Q_0$, where l_B is the Bjerrum length and $z = q/e$ the valence. Larger values of E correspond to "stiffer" dumbbells, i.e. to increased electrostatic repulsion between the beads. In the limit $E \rightarrow 0$, the original (uncharged) FENE-P model is recovered, while the dumbbells become rigid as $E \rightarrow \infty$.

Furthermore, we introduce the mean-square relative dumbbell elongation, x , as:

$$x = \frac{\langle Q^2 \rangle}{Q_0^2}. \quad (2.10)$$

Making use of pre-averaging approximations (2.7)-(2.8) and notations (2.9)-(2.10), (2.6) can be rewritten as:

$$\boldsymbol{\tau}_p = -nH \frac{\langle \mathbf{Q}\mathbf{Q} \rangle}{1 - x} + nH \frac{E}{b} \frac{\langle \mathbf{Q}\mathbf{Q} \rangle}{x^{3/2}} + nkT\boldsymbol{\delta}. \quad (2.11)$$

With the definition of the C-FENE-P Z-factor as:

$$Z = \frac{1}{1 - x} - \frac{E}{b} \frac{1}{x^{3/2}}, \quad (2.12)$$

(2.11) reduces to:

$$\boldsymbol{\tau}_p = -nHZ\langle \mathbf{Q}\mathbf{Q} \rangle + nkT\boldsymbol{\delta}. \quad (2.13)$$

Expression (2.13) is identical in form to the corresponding equation of the FENE-P dumbbell model (Bird *et al.* 1980). One can still proceed by taking the Oldroyd derivatives of both sides of the equation, eliminating $\langle \mathbf{Q}\mathbf{Q} \rangle_{(1)}$ using the Giesekus form of the stress tensor (2.5) and then eliminating $\langle \mathbf{Q}\mathbf{Q} \rangle$ using (2.13) once more. The result is:

$$\frac{b}{3}Z\boldsymbol{\tau}_p + \lambda\boldsymbol{\tau}_{p(1)} - \lambda\{\boldsymbol{\tau}_p - nkT\boldsymbol{\delta}\}D_t \ln Z = -nkT\lambda\dot{\boldsymbol{\gamma}}, \quad (2.14)$$

where $\dot{\boldsymbol{\gamma}} = (\nabla \mathbf{v}) + (\nabla \mathbf{v})^T$ is the rate-of-strain tensor, while D_t stands for the material derivative. This result is identical to the constitutive equation of the FENE-P dumbbells. Thus, the difference between the FENE-P and the C-FENE-P models is exclusively the appearance of E in the Z -factor.

Taking the trace of (2.11) and making some simple rearrangements, one arrives at:

$$Zx = \frac{3}{b} \left(1 - \frac{\text{tr } \boldsymbol{\tau}_p}{3nkT} \right). \quad (2.15)$$

Combining this with the definition of the Z -factor (2.12) leads to the following algebraic equation for x :

$$\frac{1}{1-x} - \frac{E}{b\sqrt{x}} = Z_0, \quad (2.16)$$

where

$$Z_0 = 1 + \frac{3}{b} \left(1 - \frac{\text{tr } \boldsymbol{\tau}_p}{3nkT} \right) \quad (2.17)$$

is the Z -factor of the original FENE-P dumbbell model.

In order to facilitate the solution of equation (2.16) with respect to x , we introduce $X = 1/x$. Then,

$$\frac{1}{1-x} = \frac{X}{X-1} = 1 + \frac{1}{X-1}, \quad (2.18)$$

and (2.16) becomes:

$$(Z_0 - 1) + \frac{E}{b}\sqrt{X} = \frac{1}{X-1}. \quad (2.19)$$

We further introduce $\mathcal{F}(s, \alpha)$ as the unique real solution of the equation

$$s + \alpha\sqrt{y} = \frac{1}{y-1} \quad (2.20)$$

with respect to y , assuming $\alpha \geq 0$ and $s > 0$. Some properties of this function will be used in this work. In particular, at fixed s , \mathcal{F} is a monotonically decreasing function of α ; and at fixed α , \mathcal{F} is monotonically decreasing as s increases. Furthermore, $\mathcal{F}(s, \alpha) > 1$ on its domain, with

$$\lim_{s \rightarrow \infty} \mathcal{F}(s, \alpha) = \lim_{\alpha \rightarrow \infty} \mathcal{F}(s, \alpha) = 1; \quad (2.21)$$

and finally, $\mathcal{F}(s, 0) = 1 + 1/s$. Then:

$$X = \mathcal{F}(Z_0 - 1, E/b); \quad (2.22)$$

and from (2.15):

$$Z = (Z_0 - 1)\mathcal{F}(Z_0 - 1, E/b). \quad (2.23)$$

The constitutive equations are therefore completely formulated through expressions (2.14), (2.17), and (2.23).

One observes that the C-FENE-P dumbbell model contains four parameters: (nkT) ,

b , λ , and E . Of these, the first three are precisely those of the original FENE-P dumbbell model, while E is specific to C-FENE-P and describes the intrinsic rigidity of polyelectrolyte molecules: a larger value of E implies a more rigid molecule. This parameter also accounts for salt-sensitivity of polyelectrolyte molecules, the connection between E and the actual salt concentration in the solvent being inverse: higher salinity means lower values of E , and vice versa.

Finally, we consider the rigid dumbbell limit, $E \rightarrow \infty$. From (2.20) it follows that $y \rightarrow 1$ when $\alpha \rightarrow \infty$ for a finite s . So, one has $\mathcal{F}(Z_0 - 1, \infty) = 1$ for finite Z_0 . This is in agreement with physical expectations: infinitely strong electric repulsion would extend the spring to the upper limit, so that $Q \rightarrow Q_0$ and $x \rightarrow 1$. This result leads to a new polymer fluid model with constitutive equations:

$$Z_{RDB}\boldsymbol{\tau}_p + \lambda\boldsymbol{\tau}_{p(1)} - \lambda\{\boldsymbol{\tau}_p - nkT\boldsymbol{\delta}\}D_t \ln Z_{RDB} = -nkT\lambda\dot{\boldsymbol{\gamma}}, \quad (2.24)$$

$$Z_{RDB} = 1 - \frac{\text{tr } \boldsymbol{\tau}_p}{3nkT}. \quad (2.25)$$

We shall refer to this model as the rigid dumbbell (RDB) polymer model. Another rigid dumbbell model, derived using physical assumptions different from ours, has been introduced and investigated earlier by Bird *et al.* (1971); for details, see (Bird *et al.* 1987*b*, ch. 14) and references therein. The two models share a lot of similarities, but they are not equivalent. A detailed comparison between them lies beyond the scope of the present work and shall be discussed elsewhere. In what follows, "RDB" will refer to the polymer model formulated by (2.24)-(2.25).

Note that neither H nor b appear explicitly in (2.24) and (2.25). Moreover, H , and therefore b , is not defined for the rigid dumbbells. As a result, the commonly adopted microscopic time scale λ_H is not applicable in the RDB limit; but λ_Q , defined by (2.1), is independent of H and hence provides a universal microscopic time scale for the FENE-P, C-FENE-P, and RDB models. This justifies our choice $\lambda = \lambda_Q$.

3. Steady flow material functions

In sections 3 and 4 we shall present the material functions predicted by the C-FENE-P dumbbell and RDB fluid models for some standard flow regimes. The contribution of the Newtonian solvent to the material functions is well understood; therefore, only the *polymer* contribution to the material functions will be discussed.

3.1. Steady shear flow

Steady shear flow can be locally described by a fluid velocity field given by:

$$v_1 = v_1(x_2), \quad v_2 = v_3 = 0, \quad (3.1)$$

the stress tensor and its Oldroyd derivative having the form:

$$\boldsymbol{\tau} = \begin{bmatrix} \tau_{11} & \tau_{12} & 0 \\ \tau_{12} & \tau_{22} & 0 \\ 0 & 0 & \tau_{33} \end{bmatrix} \quad \text{and} \quad \boldsymbol{\tau}_{(1)} = - \begin{bmatrix} 2\tau_{12} & \tau_{22} & 0 \\ \tau_{22} & 0 & 0 \\ 0 & 0 & 0 \end{bmatrix} \dot{\boldsymbol{\gamma}}_{12}, \quad (3.2)$$

respectively. The rate-of-strain tensor has only one independent non-zero component $\dot{\boldsymbol{\gamma}} \equiv \dot{\boldsymbol{\gamma}}_{12} = \dot{\boldsymbol{\gamma}}_{21}$, and the three standard steady shear flow material functions – non-Newtonian viscosity, η ; first normal stress coefficient, Ψ_1 ; and second normal stress coefficient, Ψ_2 –

are defined, respectively, by:

$$\tau_{12} = -\eta(\dot{\gamma})\dot{\gamma}, \quad (3.3)$$

$$N_1 = \tau_{11} - \tau_{22} = -\Psi_1(\dot{\gamma})\dot{\gamma}^2, \quad (3.4)$$

$$N_2 = \tau_{22} - \tau_{33} = -\Psi_2(\dot{\gamma})\dot{\gamma}^2, \quad (3.5)$$

where N_1 and N_2 are the first and the second normal stress difference, respectively.

Substituting (3.2) into the constitutive equation (2.14) yields:

$$\frac{b}{3}Z\tau_{11} = 2\lambda\tau_{12}\dot{\gamma}, \quad (3.6)$$

$$\frac{b}{3}Z\tau_{12} = -nkT\lambda\dot{\gamma}, \quad (3.7)$$

$$\tau_{22} = \tau_{33} = 0. \quad (3.8)$$

In all but the form of Z , these equations are identical to those arising in the FENE-P dumbbell model. It follows from (3.6)-(3.7) that Ψ_1 is directly proportional to the square of the viscosity, the coefficient of proportionality being independent of E ; and, according to (3.8), Ψ_2 vanishes identically:

$$\Psi_1(\dot{\gamma}) = \frac{2}{nkT}\eta^2(\dot{\gamma}), \quad (3.9)$$

$$\Psi_2(\dot{\gamma}) = 0. \quad (3.10)$$

Having eliminated τ_{11} from (3.6)-(3.7), one arrives at the following non-linear algebraic relation between the shear stress and the shear rate:

$$\left(1 + \frac{2\mathcal{T}_{12}^2}{3}\right)\mathcal{F}\left(\frac{3 + 2\mathcal{T}_{12}^2}{b}, \frac{E}{b}\right)\mathcal{T}_{12} = -\lambda\dot{\gamma}, \quad (3.11)$$

where $\mathcal{T}_{12} = \tau_{12}/(nkT)$. Equation (3.11) can be solved numerically to calculate steady shear flow properties of the C-FENE-P dumbbells for arbitrary values of b and E .

The influence of E on the relative elongation of the dumbbells in steady shear flow is shown in figure 1, left. In general, a higher value of E leads to larger spring extensions, as expected. This effect is very pronounced at equilibrium and at low-to-medium shear rates. At higher shear rates, the dumbbells are stretched almost to the upper limit by the flow, so that the influence of E becomes small.

The predicted impact of salinity on the non-Newtonian viscosity is shown in figure 1, right. The C-FENE-P dumbbells demonstrate shear-thinning behaviour, which is typical for polymer solutions. Decreasing E , which is equivalent to increasing the solvent salinity, leads to two noticeable effects. Firstly, the non-Newtonian viscosity decreases at fixed shear rate values. The relative reduction in viscosity is largest at small shear rates and decreases as the shear rate increases, vanishing when $\dot{\gamma} \rightarrow \infty$. Secondly, the onset of shear-thinning is shifted towards higher shear rates.

The asymptotic behaviour of the viscosity curves governed by (3.11) can be studied analytically. At very low shear rates, the viscosity approaches its zero-shear-rate value

$$\eta_0 = \frac{nkT\lambda}{\mathcal{F}(3/b, E/b)}, \quad (3.12)$$

which is highly sensitive to E . In the FENE-P limit ($E = 0$), this result simplifies to:

$$\eta_{0, FENE} = \frac{3}{b+3}nkT\lambda; \quad (3.13)$$

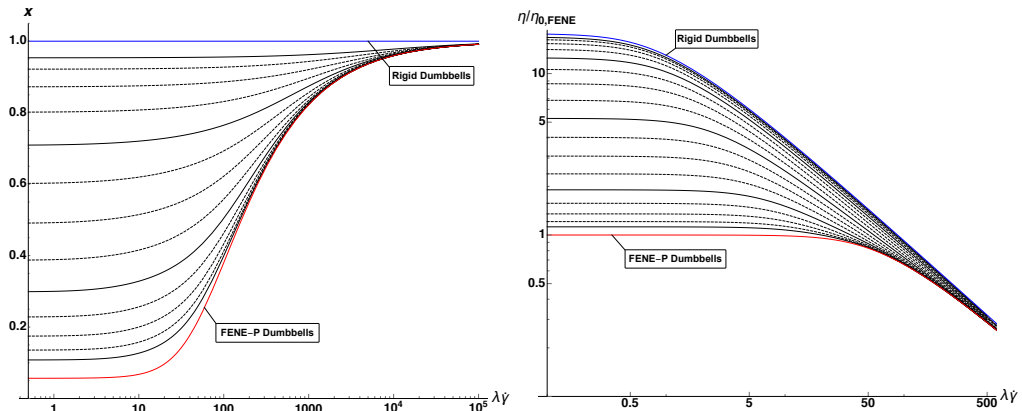


FIGURE 1. The mean-square relative elongation x in steady shear flow (left) and the scaled polymer contribution to the non-Newtonian viscosity (right), as predicted by the C-FENE-P dumbbell model. Both are plotted as functions of the dimensionless shear rate $\lambda\dot{\gamma}$. The viscosity is scaled with respect to the zero-shear-rate viscosity of the FENE-P dumbbells. Different curves correspond to different values of E . The coloured lines show the limiting cases $E = 0$ and $E \rightarrow \infty$. The black lines are drawn at $\log_{10} E$ varying from 0 to 3 (left) and from -1 to 3 (right) with a step of 0.25, bottom up; the solid black lines correspond to integer values of $\log_{10} E$. The value of the non-linearity parameter, b , is set to a moderate value of 50.

and in the RDB limit ($E \rightarrow \infty$), the zero-shear-rate viscosity is:

$$\eta_{0, RDB} = nkT\lambda. \quad (3.14)$$

At very high shear rates, the asymptotic behaviour of the viscosity curves in the RDB, C-FENE-P, and FENE-P models is identical, independent of E , and described by:

$$\eta \approx \sqrt[3]{\frac{3}{2}} nkT\lambda (\lambda\dot{\gamma})^{-2/3}. \quad (3.15)$$

Finally, in the FENE-P and RDB limits, exact analytical solutions of (3.11) can be obtained. That for the FENE-P dumbbells is can be found, e.g. in (Shogin *et al.* 2017). In the RDB limit, (3.11) reduces to the following cubic equation for \mathcal{T}_{12} :

$$\left(1 + \frac{2\mathcal{T}_{12}^2}{3}\right) \mathcal{T}_{12} = -\lambda\dot{\gamma}. \quad (3.16)$$

This equation has one real solution, which can be obtained, e.g. using the methods described by La Nave & Mazur (2002). The result can be written as:

$$\frac{\eta_{RDB}}{\eta_{0, RDB}} = \frac{-2^{1/3} + \left(3\Lambda + \sqrt{2 + 9\Lambda^2}\right)^{2/3}}{2^{2/3}\Lambda \left(3\Lambda + \sqrt{2 + 9\Lambda^2}\right)^{1/3}}, \quad (3.17)$$

where $\Lambda = \lambda\dot{\gamma}$ is the dimensionless shear rate.

3.2. Steady shearfree flow

The steady simple shearfree flow velocity field is:

$$v_1 = -\frac{1}{2}\dot{\epsilon}x_1, \quad v_2 = -\frac{1}{2}\dot{\epsilon}x_2, \quad v_3 = \dot{\epsilon}x_3, \quad (3.18)$$

where $\dot{\epsilon}$ is the time-independent elongation rate, which can take positive and negative values. At $\dot{\epsilon} > 0$, the flow is called elongational; at $\dot{\epsilon} < 0$, it is referred to as biaxial stretching.

The rate-of-strain tensor, the stress tensor, and the Oldroyd derivative of the latter are all diagonal:

$$\dot{\gamma} = \text{diag}(-\dot{\epsilon}, -\dot{\epsilon}, 2\dot{\epsilon}), \quad (3.19)$$

$$\tau = \text{diag}(\tau_{11}, \tau_{22}, \tau_{33}), \quad (3.20)$$

$$\tau_{(1)} = \text{diag}(\tau_{11}, \tau_{22}, -2\tau_{33})\dot{\epsilon}, \quad (3.21)$$

with $\tau_{11} = \tau_{22}$ due to the flow symmetry. The only material function characterising the fluid in this type of flow is the elongational, or extensional, viscosity. Following Bird *et al.* (1987a, §3.5), we denote it by $\bar{\eta}$ and define by:

$$\tau_{33} - \tau_{11} = -\bar{\eta}(\dot{\epsilon})\dot{\epsilon}. \quad (3.22)$$

Substituting (3.19)-(3.21) into the constitutive equation (2.14) leads to:

$$\frac{b}{3}Z\tau_{11} + \lambda\dot{\epsilon}\tau_{11} = nkT\lambda\dot{\epsilon}, \quad (3.23)$$

$$\frac{b}{3}Z\tau_{33} - 2\lambda\dot{\epsilon}\tau_{33} = -2nkT\lambda\dot{\epsilon}. \quad (3.24)$$

Having replaced τ_{11} , τ_{33} , and $\dot{\epsilon}$ with dimensionless quantities

$$\mathcal{T} = \frac{2\tau_{11} + \tau_{33}}{nkT}, \quad (3.25)$$

$$\mathcal{D} = \frac{\tau_{11} - \tau_{33}}{nkT}, \quad (3.26)$$

$$\Lambda = \lambda\dot{\epsilon}, \quad (3.27)$$

one arrives after simple rearrangements at:

$$\frac{b}{3}Z\mathcal{T} + 2\Lambda\mathcal{D} = 0, \quad (3.28)$$

$$\frac{b}{3}Z\mathcal{D} + \Lambda(\mathcal{T} - \mathcal{D}) = 3\Lambda. \quad (3.29)$$

Equations (3.28)-(3.29) can be solved by standard numerical methods. The impact of E on the elongational viscosity of the C-FENE-P dumbbells is illustrated in figure 2, right. It can be seen that the C-FENE-P dumbbells show elongational thickening at $\dot{\epsilon} > 0$. An increase in salinity (hence, a decrease in E) leads to an overall drop in the elongational viscosity. The local minimum in $\bar{\eta}$ at negative elongation rates, which vanishes in the RDB limit, becomes more pronounced as salinity increases.

One can also keep track of the mean-square relative elongation, x , which is shown in figure 2, left. The elongation is smallest at equilibrium and follows the trends similar to those of $\bar{\eta}$ at $\dot{\epsilon} > 0$.

Some properties of the elongational viscosity curves can be obtained by analytical means. In particular, (3.29) can be used to calculate $\bar{\eta}_0$, the elongational viscosity at zero elongation rate. Considering the limit $\dot{\epsilon} \rightarrow 0$ and using (3.12) and (3.22) yields the relation $\bar{\eta}_0 = 3\eta_0$, which also holds for Newtonian fluids.

At very large positive or negative elongation rates (in the limit $|\dot{\epsilon}| \rightarrow \infty$), the relative extension of the dumbbells approaches one; hence, the asymptotic behaviour of the C-FENE-P and FENE-P dumbbells must be identical to that of the RDB model. In the

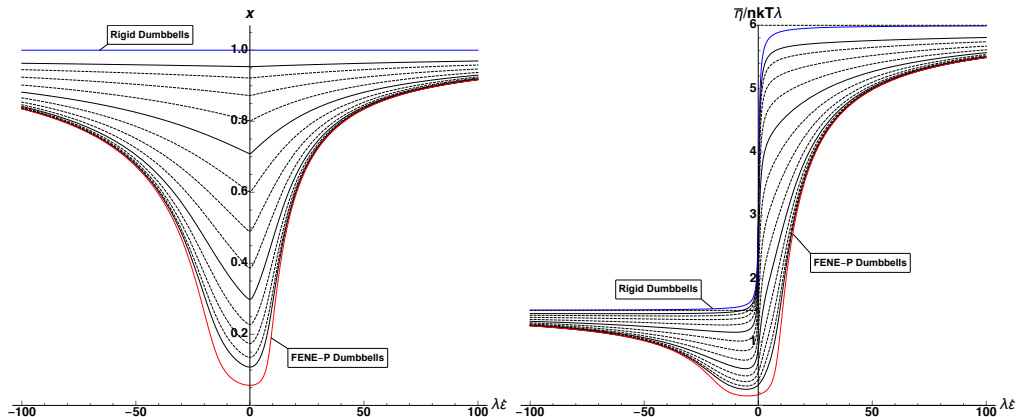


FIGURE 2. The mean-square relative elongation x in steady elongational flow (left) and the scaled polymer contribution to the elongational viscosity (right) of the C-FENE-P dumbbells, plotted as a function of the dimensionless elongation rate $\lambda\dot{\epsilon}$. Different curves correspond to different values of E : $E = 0$ and $E \rightarrow \infty$ (coloured lines); and $\log_{10} E$ varying from 0 to 3 with a step of 0.25 (black lines bottom up, solid lines corresponding to integer values of $\log_{10} E$). The value of non-linearity parameter $b = 50$.

RDB limit, equations (3.28)-(3.29) become:

$$\left(1 - \frac{\mathcal{T}}{3}\right) \mathcal{T} + 2\Lambda \mathcal{D} = 0, \quad (3.30)$$

$$\left(1 - \frac{\mathcal{T}}{3}\right) \mathcal{D} + \Lambda(\mathcal{T} - \mathcal{D}) = 3\Lambda. \quad (3.31)$$

This system has three solutions, of which only one:

$$\mathcal{T} = \frac{3}{2} \left(1 - \Lambda - \sqrt{1 - 2\Lambda + 9\Lambda^2}\right), \quad (3.32)$$

$$\mathcal{D} = \frac{3}{4} \left(-1 + 5\Lambda + \sqrt{1 - 2\Lambda + 9\Lambda^2}\right), \quad (3.33)$$

provides $\mathcal{T} = \mathcal{D} = 0$ at equilibrium ($\Lambda = 0$) and hence is physically relevant. It is seen that at $\Lambda \rightarrow \infty$, $\mathcal{D} \sim 6\Lambda$, and at $\Lambda \rightarrow -\infty$, $\mathcal{D} \sim 3/2\Lambda$. This means that for all the models under consideration (FENE-P, C-FENE-P, and RDB), $\bar{\eta}$ approaches $\bar{\eta}_{+\infty} = 6nkT\lambda$ at large positive elongation rates and $\bar{\eta}_{-\infty} = (3/2)nkT\lambda$ at large negative elongation rates. Equation (3.33) also provides an exact analytical expression for the elongational viscosity in the RDB limit:

$$\frac{\bar{\eta}(\Lambda)}{\bar{\eta}_{0, RDB}} = \frac{-1 + 5\Lambda + \sqrt{1 - 2\Lambda + 9\Lambda^2}}{4\Lambda}. \quad (3.34)$$

4. Transient shear flow material functions

4.1. Small-amplitude oscillatory shear flow

In small-amplitude oscillatory shear (SAOS) flow, the fluid velocity field is given by:

$$v_1 = \dot{\gamma}_{12}(t)x_2, \quad v_2 = v_3 = 0, \quad (4.1)$$

where the harmonically oscillating shear rate

$$\dot{\gamma}_{12}(t) = \dot{\gamma}_{21}(t) = \dot{\gamma}_0 \cos(\omega t) \quad (4.2)$$

is the only independent non-zero component of the rate-of-strain tensor. Here $\dot{\gamma}_0$ is the amplitude of oscillations, and ω is the angular frequency. The latter is assumed very small, so that the dependency of the stress tensor components on $\dot{\gamma}_0$ is completely described by the lowest-order terms (first order for the shear stresses and second for the normal stresses). The stress tensor of a fluid undergoing SAOS flow has the general form

$$\boldsymbol{\tau}(t) = \begin{bmatrix} \tau_{11}(t) & \tau_{12}(t) & 0 \\ \tau_{12}(t) & \tau_{22}(t) & 0 \\ 0 & 0 & \tau_{33}(t) \end{bmatrix}, \quad (4.3)$$

with

$$\boldsymbol{\tau}_{(1)} = \partial_t \boldsymbol{\tau} - \begin{bmatrix} 2\tau_{12}(t) & \tau_{22}(t) & 0 \\ \tau_{22}(t) & 0 & 0 \\ 0 & 0 & 0 \end{bmatrix} \dot{\gamma}_{12}(t). \quad (4.4)$$

For polymer solutions, the shear stress oscillates around zero with frequency ω ; however, on the contrast to Newtonian liquids, the oscillations are not in phase with those of the shear rate. The normal stress differences oscillate around generally non-zero mean values with the double frequency 2ω (Bird *et al.* 1987a, §3.4). The properties of the fluid in SAOS flow are then described by eight material functions – η' , η'' ; Ψ_1^d , Ψ_1' , Ψ_1'' ; and Ψ_2^d , Ψ_2' , Ψ_2'' – defined by:

$$\tau_{12} = -\eta'(\omega)\dot{\gamma}_0 \cos(\omega t) - \eta''(\omega)\dot{\gamma}_0 \sin(\omega t), \quad (4.5)$$

$$N_1 = -\Psi_1^d(\omega)\dot{\gamma}_0^2 - \Psi_1'(\omega)\dot{\gamma}_0^2 \cos(2\omega t) - \Psi_1''(\omega)\dot{\gamma}_0^2 \sin(2\omega t), \quad (4.6)$$

$$N_2 = -\Psi_2^d(\omega)\dot{\gamma}_0^2 - \Psi_2'(\omega)\dot{\gamma}_0^2 \cos(2\omega t) - \Psi_2''(\omega)\dot{\gamma}_0^2 \sin(2\omega t). \quad (4.7)$$

Six of these functions are often combined to form the complex quantities $\eta' + i\eta''$ (complex viscosity), $\Psi_1' + i\Psi_1''$, and $\Psi_2' + i\Psi_2''$ (complex first and second normal stress coefficient, respectively); while Ψ_1^d and Ψ_2^d are the first and the second normal stress displacement coefficients.

The in-phase ("real") viscosity component, η' , describes the direct response of the fluid and can be associated with energy loss due to dissipation. The out-of-phase ("imaginary") component, η'' , arises because the long polymer molecules do not react instantly to rapid flow changes. This leads to a latency, described by a phase shift. This latency can be interpreted as "elasticity" of the flow and associated with energy storage (Ferry 1980; Mezger 2014). The complex viscosity components, η' and η'' can also be replaced by the storage and loss moduli, G' and G'' , defined, respectively, by:

$$G' = \eta''\omega, \quad G'' = \eta'\omega. \quad (4.8)$$

These ("elastic") moduli are often measured in experiments.

The expressions for the SAOS flow material functions of the C-FENE-P dumbbells can be obtained analytically. Substituting (4.3)-(4.4) into the constitutive equation (2.14), keeping only the lowest-order terms in $\dot{\gamma}_{12}$, combining and rearranging the scalar equations, one gets:

$$N_1 + \lambda_e \partial_t N_1 - 2\lambda_e \tau_{12} \dot{\gamma}_{12} = 0, \quad (4.9)$$

$$N_2 + \lambda_e \partial_t N_2 = 0, \quad (4.10)$$

$$\tau_{12} + \lambda_e \partial_t \tau_{12} = -\eta_0 \dot{\gamma}_{12}, \quad (4.11)$$

where we have introduced the "experimental" time constant λ_e by

$$\lambda_e(b, E) = \frac{\eta_0}{nkT} = \frac{\lambda}{\mathcal{F}(3/b, E/b)}, \quad (4.12)$$

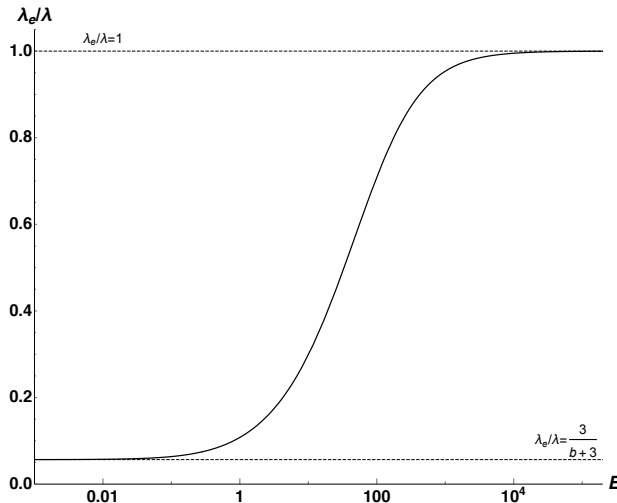


FIGURE 3. The dependency of the experimental time constant of the C-FENE-P dumbbells, λ_e , on E . For illustrative purpose, the value of b is set to 50.

with η_0 as the zero-shear-rate viscosity of the C-FENE-P dumbbells given by (3.12). As shown in figure 3, this time constant is a monotonically increasing function of E , ranging from $3\lambda/(b+3)$ at $E=0$ to λ at $E \rightarrow \infty$.

Substituting (4.5)-(4.7) turn equations (4.9)-(4.11) into identities which hold for all values of (ωt) . This leads to eight algebraic equations for the material functions. Then, the SAOS flow material functions can be written in scaled form as functions of the dimensionless frequency, $\Lambda_e = \lambda_e \omega$. The linear viscoelastic response is:

$$\frac{\eta'}{\eta_0} = \frac{1}{1 + \Lambda_e^2}, \quad \frac{\eta''}{\eta_0} = \frac{\Lambda_e}{1 + \Lambda_e^2}, \quad (4.13)$$

$$\frac{G'}{nkT} = \frac{\Lambda_e^2}{1 + \Lambda_e^2}, \quad \frac{G''}{nkT} = \frac{\Lambda_e}{1 + \Lambda_e^2}, \quad (4.14)$$

which is identical to that of a Maxwell fluid with viscosity $nkT\lambda_e$ and time constant λ_e (Bird *et al.* 1987a, §5.2–5.3). The material functions related to $N_2 - \Psi_2^d$, Ψ_2' , and Ψ_2'' – all vanish, while N_1 is described by:

$$\frac{\Psi_1^d}{\Psi_{1,0}} = \frac{1}{2(1 + \Lambda_e^2)}, \quad (4.15)$$

$$\frac{\Psi_1'}{\Psi_{1,0}} = \frac{1 - 2\Lambda_e^2}{2(1 + \Lambda_e^2)(1 + 4\Lambda_e^2)}, \quad (4.16)$$

$$\frac{\Psi_1''}{\Psi_{1,0}} = \frac{3\Lambda_e}{2(1 + \Lambda_e^2)(1 + 4\Lambda_e^2)}, \quad (4.17)$$

where $\Psi_{1,0} = 2nkT\lambda_e^2$ is the zero-shear-rate first normal stress coefficient of the C-FENE-P dumbbells. The scaled material functions, given by equations (4.15)-(4.17), are shown in figure 4, where they are plotted against Λ_e .

The first normal stress displacement coefficient, Ψ_1^d , is a decreasing function of frequency. At low frequencies, $\Psi_1^d \rightarrow \Psi_{1,0}/2$; and at high frequencies, $\Psi_1^d \sim \omega^{-2}$.

The real component of the complex first normal stress coefficient, Ψ_1' , is the only SAOS material function of the C-FENE-P model which can take negative values. At very low frequencies, $\Psi_1' \rightarrow \Psi_{1,0}/2$. At low-to-moderate frequencies, Ψ_1' decreases with frequency,

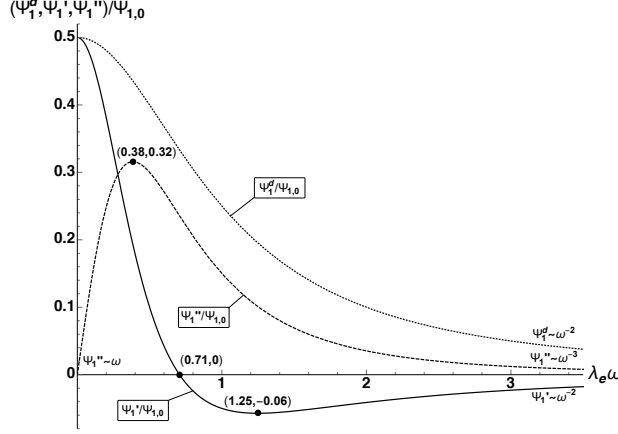


FIGURE 4. The scaled polymer contribution to the material functions describing the first normal stress difference of the C-FENE-P dumbbells in SAOS flow, plotted against the experimental dimensionless frequency $\lambda_e \omega$.

becoming zero at $\Lambda_e = 1/\sqrt{2} \approx 0.707$, and continues to decline until the minimum point

$$\Psi_1' = \left(\frac{2\sqrt{2}}{3} - 1 \right) \Psi_{1,0} \approx -0.057 \Psi_{1,0} \quad (4.18)$$

is reached at

$$\Lambda_e = \left[\frac{3 + \sqrt{2}}{2\sqrt{2}} \right]^{1/2} \approx 1.249. \quad (4.19)$$

Thereafter, Ψ_1' starts to increase with frequency, approaching zero from below, with $\Psi_1' \sim \omega^{-2}$ at high frequencies.

The imaginary component of the complex first normal stress coefficient, Ψ_1'' , increases linearly at low frequencies ($\Psi_1'' \sim \omega$), reaching a maximum value of

$$\Psi_1'' = \frac{9 [3(\sqrt{73} - 5)/2]^{1/2}}{23 + 5\sqrt{73}} \Psi_{1,0} \approx 0.316 \Psi_{1,0} \quad (4.20)$$

at

$$\Lambda_e = \frac{1}{2} \left[\frac{\sqrt{73} - 5}{6} \right]^{1/2} \approx 0.384, \quad (4.21)$$

and decays quickly at large frequencies ($\Psi_1'' \sim \omega^{-3}$).

Expressions (4.13)-(4.17) show that the SAOS material functions of the C-FENE-P, FENE-P, and RDB fluid models can be written in the same form. However, this form is not suitable for visualising the impact of E , since all the scaling factors depend on E . To investigate the E -dependence, we reformulate (4.13)-(4.17) using salinity-independent scaling factors: the zero-shear-rate viscosity and the zero-shear-rate first normal stress coefficient of the FENE-P dumbbells, $\eta_{0, FENE}$ and $\Psi_{1,0, FENE}$, in place of η_0 and $\Psi_{1,0}$; and λ in place of λ_e .

The dependence of the in-phase complex viscosity component on E is shown in figure 5, top left. It is seen that a decrease in E leads to a reduction in η' at lower frequencies, but to an increase in η' at higher frequencies; and the onset of "frequency-thinning" is shifted towards higher frequency values as E decreases.

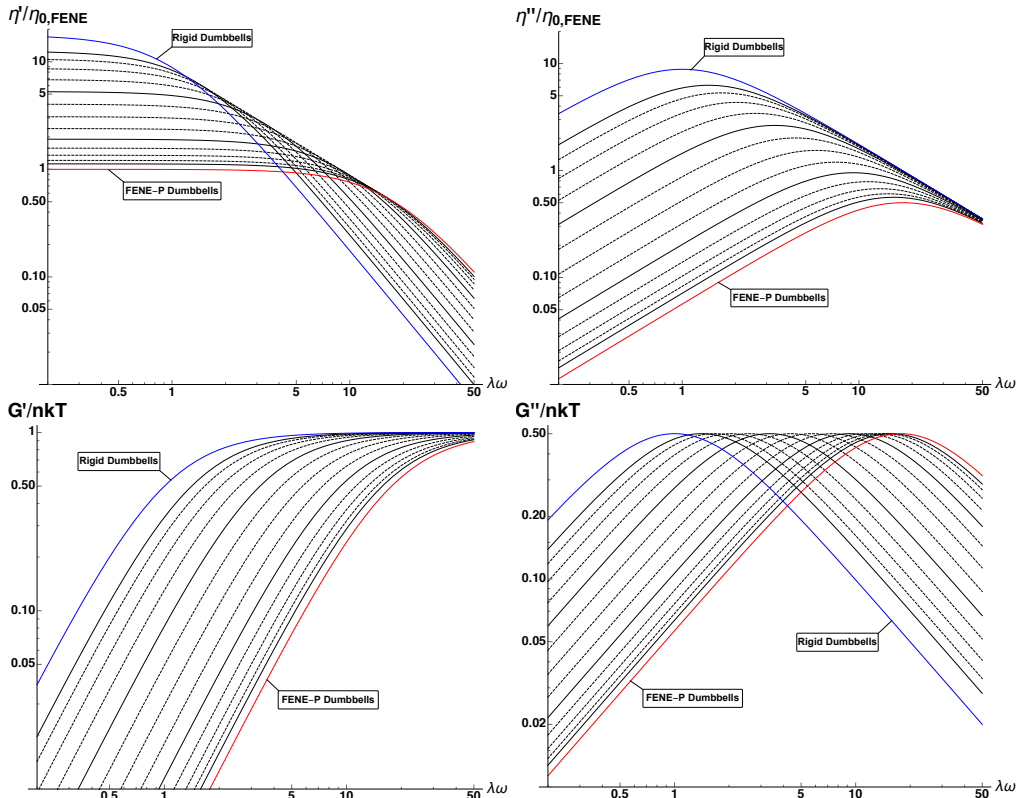


FIGURE 5. The scaled polymer contribution to the complex viscosity components (top) and to the elastic moduli (bottom) of the C-FENE-P dumbbell solution undergoing SAOS flow, plotted against the dimensionless frequency $\lambda\omega$. Both components are scaled with respect to the zero-shear-rate viscosity of the FENE-P dumbbells. The curves for different values of E are shown: $E = 0$ and $E \rightarrow \infty$ (coloured lines); and $\log_{10} E$ varying from -1 to 2 with a step of 0.25 (black lines bottom up at low frequencies, solid lines corresponding to integer values of $\log_{10} E$). The non-linearity parameter $b = 50$.

The impact of E on the out-of-phase complex viscosity component is visualised in figure 5, top right. A decrease in E mostly affects the low- and mid-frequency regions of the curves: the values of η'' are reduced, and the maximum is shifted towards higher frequencies. At very high frequencies, E has no effect on η'' : the curves of the C-FENE-P, FENE-P, and RDB models are asymptotically identical.

The storage and loss moduli are found to depend on E in a simple way, see figure 5, bottom. If the curves are plotted using a log-log scale, a reduction in E results in a translation of both G' and G'' curves to the right due to a decrease in the time constant; the maximum values of both moduli thus remain unchanged.

The E -dependence of the SAOS material functions related to N_1 is shown in figure 6. At low and moderate frequencies, Ψ_1^d is affected in a way similar to η (figure 6, bottom), and Ψ_1'' – similar to η'' (figure 6, top right). The impact of E on Ψ_1' is more complex, but still follows the same general trend: A decrease in E leads to an overall reduction in the magnitude of Ψ_1' and shifts the characteristic points towards higher frequencies (figure 6, top left). At high frequencies, all three material functions are insensitive to E .

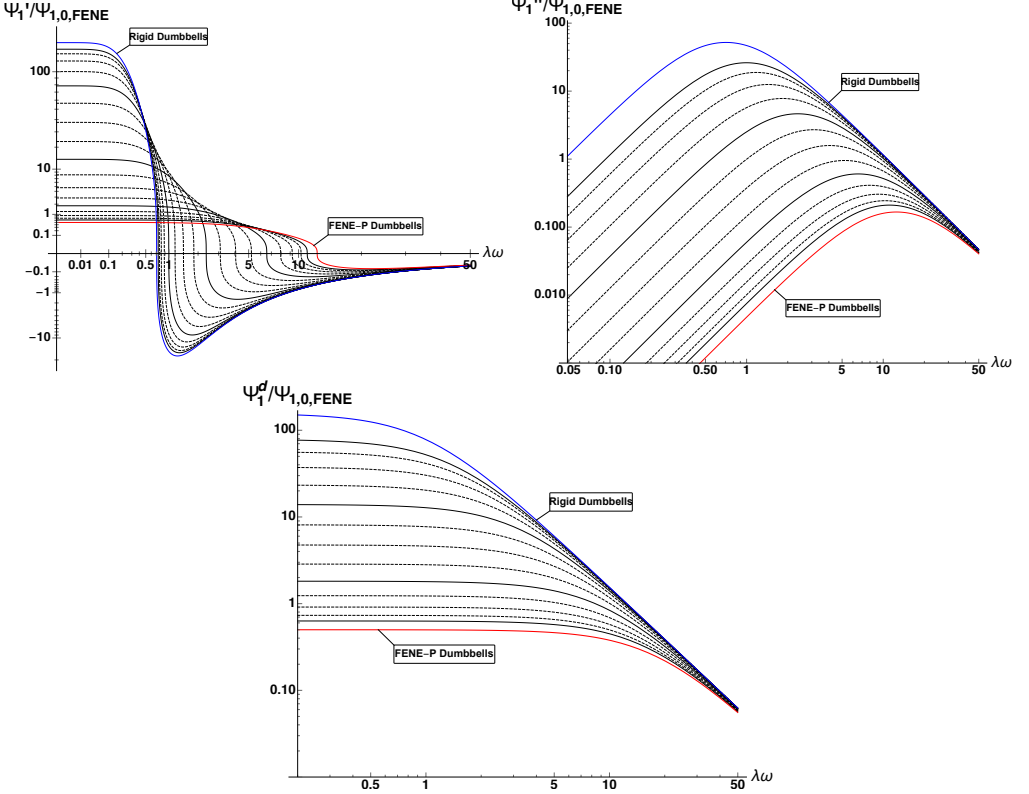


FIGURE 6. The scaled complex first normal stress coefficient components (top) and first normal stress displacement coefficient (bottom) of the C-FENE-P dumbbells, plotted against the dimensionless frequency $\lambda\omega$. The coloured lines show the cases $E = 0$ and $E \rightarrow \infty$. The black lines are drawn at $\log_{10} E$ varying from -1 to 2 with a step of 0.25 , bottom up at low frequencies; solid black lines correspond to integer values of $\log_{10} E$. The curves are plotted at $b = 50$. Both axes on the top left plot are scaled with a cubic root function, since Ψ'_1 changes its sign.

4.2. Start-up and cessation of steady shear flow

Start-up and cessation of steady shear flow are two closely related transient shear flows. The velocity field in these flows is described by (4.1); the stress tensor and its Oldroyd derivative are given by (4.3)-(4.4); while the only independent non-zero component of the rate-of-strain tensor is:

$$\dot{\gamma}(t) \equiv \dot{\gamma}_{12}(t) = \dot{\gamma}_{21}(t) = \dot{\gamma}_0 H(\pm t), \quad (4.22)$$

where $\dot{\gamma}_0$ is a constant, and $H(t)$ is the Heaviside step-function; by this reason, these flows are known in experimental rheology as step-rate tests, see e.g. (Mezger 2014).

Choosing the positive sign in (4.22) corresponds to the start-up case. The fluid is at rest at $t < 0$; a constant shear rate $\dot{\gamma}_0$ is suddenly applied at $t = 0$; and after a while, shear and normal stresses build up and reach their steady shear flow values.

On the contrast, the negative sign in (4.22) yields the cessation case, which is the inverse situation. The fluid undergoes steady shear flow with constant shear rate $\dot{\gamma}_0$ at $t < 0$; the flow is instantaneously stopped (the shear rate is removed) at $t = 0$; and the stresses decay after some time, as the fluid returns to equilibrium.

The material functions of the fluid in this kind of flow – η^\pm , Ψ_1^\pm , and Ψ_2^\pm – are defined

by:

$$\tau_{12} = -\eta^\pm(\dot{\gamma}_0, t)\dot{\gamma}_0, \quad (4.23)$$

$$N_1 = -\Psi_1^\pm(\dot{\gamma}_0, t)\dot{\gamma}_0^2, \quad (4.24)$$

$$N_2 = -\Psi_2^\pm(\dot{\gamma}_0, t)\dot{\gamma}_0^2, \quad (4.25)$$

and are known as the shear stress, first, and second normal stress difference growth (+) or relaxation (−) functions, respectively. When presented graphically, these material functions are commonly normalised using their steady-state values $\eta(\dot{\gamma}_0)$, $\Psi_1(\dot{\gamma}_0)$, and $\Psi_2(\dot{\gamma}_0)$.

Substituting (4.3)-(4.4) into the constitutive equation of the C-FENE-P dumbbells (2.14), introducing dimensionless quantities

$$\mathcal{T}_{12} = \frac{\tau_{12}}{nkT}, \quad (4.26)$$

$$\mathcal{T} = \frac{\tau_{11} + \tau_{22} + \tau_{33}}{nkT}, \quad (4.27)$$

$$\mathcal{D}_1 = \frac{N_1}{nkT}, \quad (4.28)$$

$$\mathcal{D}_2 = \frac{N_2}{nkT}, \quad (4.29)$$

$$\bar{t} = t/\lambda, \quad (4.30)$$

$$\Lambda(\bar{t}) = \lambda\dot{\gamma}_0 H(\pm\bar{t}), \quad (4.31)$$

and rearranging leads to the following system of ordinary differential equations:

$$\frac{b}{3}Z\mathcal{T}_{12} + \partial_{\bar{t}}\mathcal{T}_{12} - \mathcal{T}_{12}\partial_{\bar{t}}\ln Z = -\Lambda(\bar{t}), \quad (4.32)$$

$$\frac{b}{3}Z\mathcal{T} + \partial_{\bar{t}}\mathcal{T} - (\mathcal{T} - 3)\partial_{\bar{t}}\ln Z - 2\mathcal{T}_{12}\Lambda(\bar{t}) = 0, \quad (4.33)$$

$$\frac{b}{3}Z\mathcal{D}_1 + \partial_{\bar{t}}\mathcal{D}_1 - \mathcal{D}_1\partial_{\bar{t}}\ln Z - 2\mathcal{T}_{12}\Lambda(\bar{t}) = 0, \quad (4.34)$$

$$\frac{b}{3}Z\mathcal{D}_2 + \partial_{\bar{t}}\mathcal{D}_2 - \mathcal{D}_2\partial_{\bar{t}}\ln Z = 0. \quad (4.35)$$

The expression for the Z -factor, (2.23), completes the system. The initial conditions can be imposed at any fixed $\bar{t} < 0$, where the stress tensor components are set to zero (start-up case) or to their steady shear flow values (cessation case).

Since $\mathcal{D}_2 = 0$ both in equilibrium and in steady shear flow (see section 3.1), it follows from (4.35) that $\mathcal{D}_2(\bar{t}) = 0$ identically. The rest of the system can be solved numerically. We are using the standard methods implemented in Wolfram Mathematica for this purpose.

The results for the start-up case are shown in figure 7. At very low values of $\lambda\dot{\gamma}_0$ the material functions grow monotonically, approaching their steady-state values (figure 7, top). At higher $\lambda\dot{\gamma}_0$, they typically undergo one or several oscillations around the steady-state value before they stabilise; and a stress overshoot, i.e. a time interval where the stresses are higher than their steady-state values, is clearly seen (figure 7, middle and bottom). At the same time, the overshoot is not observed in the RDB limit. This phenomenon can be explained by dumbbell stretching: When a large shear rate is suddenly imposed, the extension of elastic dumbbells for some time exceeds its steady-flow value, while this does not happen for rigid dumbbells, which are not extended by the flow at all. Also, it is seen that at higher $\lambda\dot{\gamma}_0$, the relative magnitude of overshoots

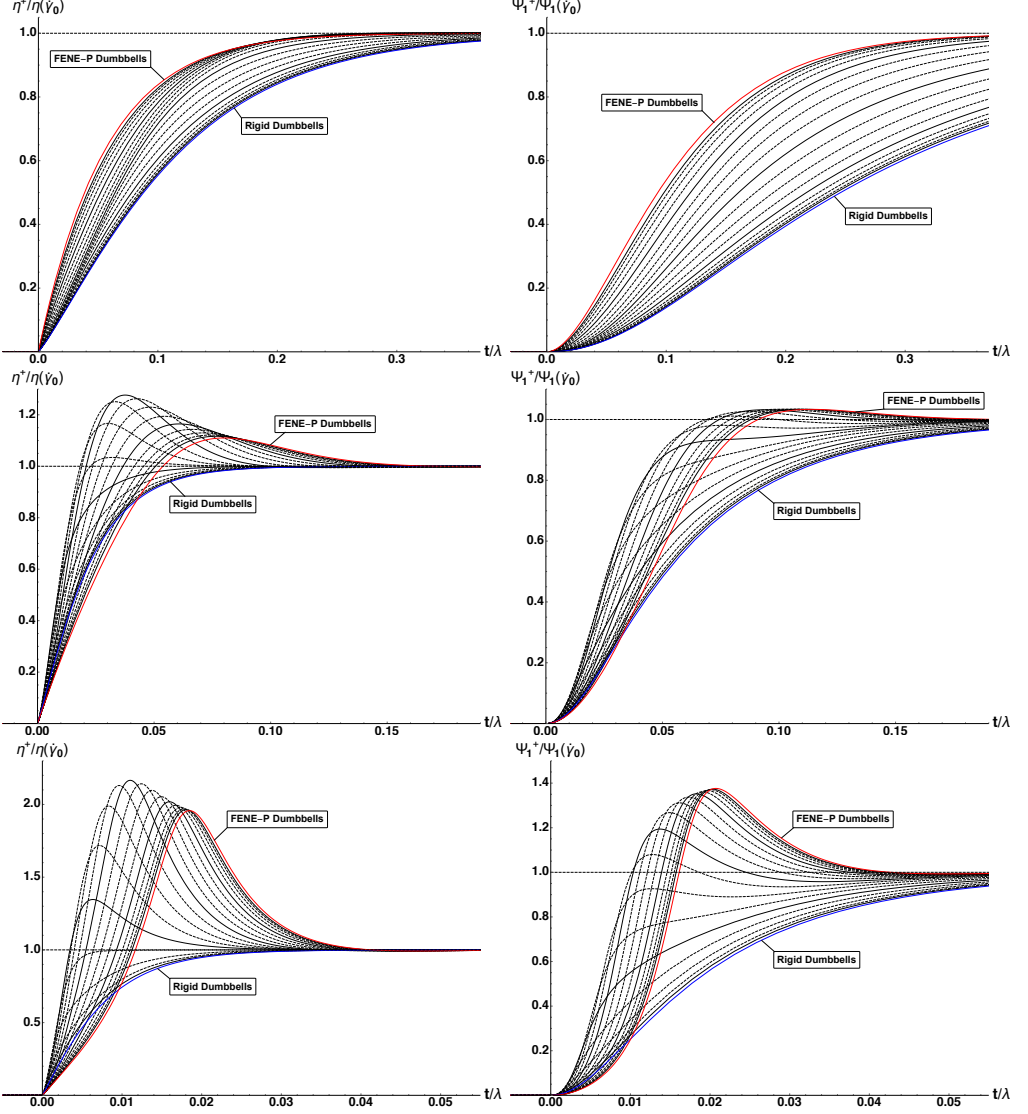


FIGURE 7. The normalised polymer contribution to the shear stress (left) and first normal stress difference (right) growth functions of the C-FENE-P dumbbells, plotted against the dimensionless time t/λ at $\lambda\dot{\gamma}_0 = 10$ (top); $\lambda\dot{\gamma}_0 = 100$ (middle); and $\lambda\dot{\gamma}_0 = 500$ (bottom). The coloured lines show the limiting cases $E = 0$ and $E \rightarrow \infty$. The black lines are drawn at $\log_{10} E$ varying from -1 to 3 with a step of 0.25 , bottom up at late times; solid black lines correspond to integer values of $\log_{10} E$. All curves are plotted at $b = 50$.

increases and their points of maximum are shifted towards earlier times; it takes less time for the stresses to approach their steady-state values; and for any fixed $\lambda\dot{\gamma}_0$, the shear stress builds up and stabilises faster than N_1 .

The material functions describing the start-up case depend strongly on E . At low $\lambda\dot{\gamma}_0$, a decrease in E results in a general increase in $\eta^+/\eta(\dot{\gamma}_0)$ and $\Psi_1^+/\Psi_1(\dot{\gamma}_0)$ (figure 7, top). At higher values of $\lambda\dot{\gamma}_0$, the impact of E becomes more complex. Firstly, a shear stress overshoot appears (figure 7, middle left and bottom left). As E decreases, the overshoot is shifted towards later times. At the same time, the overshoot magnitude increases, passes

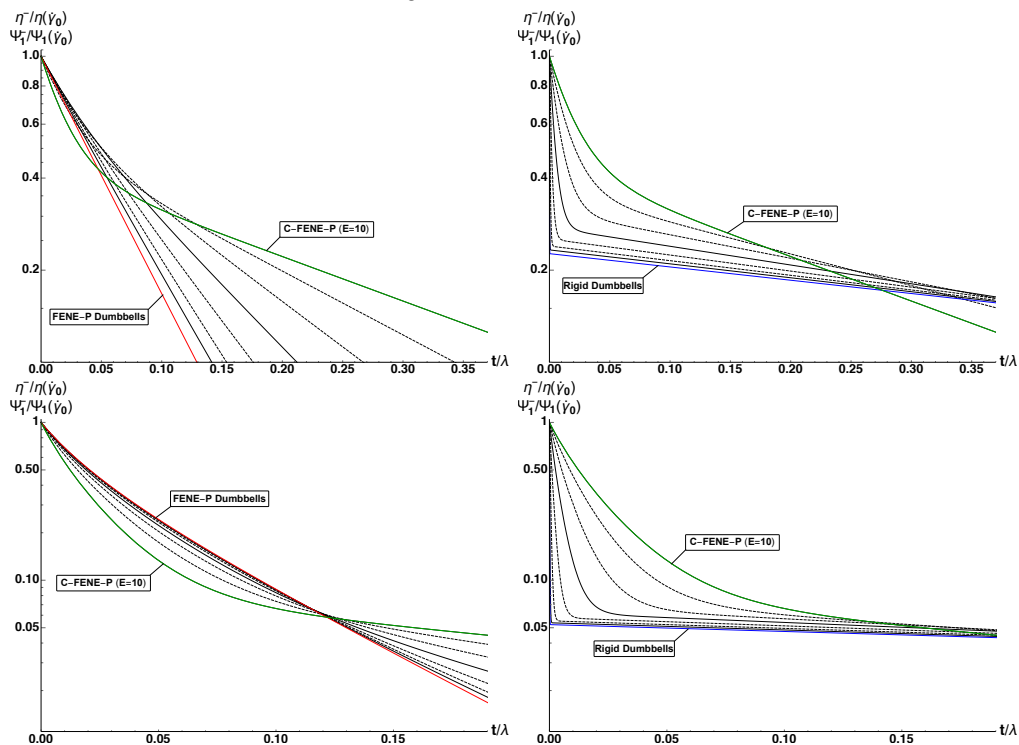


FIGURE 8. The normalised polymer contribution to the shear stress and first normal stress difference relaxation functions of C-FENE-P dumbbells, plotted against dimensionless time t/λ at $\lambda\dot{\gamma}_0 = 10$ (top) and $\lambda\dot{\gamma}_0 = 100$ (bottom). The coloured lines show the FENE-P limit $E = 0$, the RDB limit $E \rightarrow \infty$, and the case when $E = 10$. The black lines are drawn at $\log_{10} E$ varying from -1 to $2/3$ (left) and from $4/3$ to 3 (right), with a step of $1/3$; solid black lines correspond to integer values of $\log_{10} E$. The value of b is set to 50.

a maximum, and then decreases, reaching its final value in the FENE-P dumbbell limit ($E = 0$). The situation is qualitatively similar for N_1 (figure 7, middle right and bottom right); however, the N_1 overshoot magnitude increases monotonically as E decreases, reaching its maximal value at $E = 0$.

In other words, an increase in solvent salinity can either increase or decrease the relative shear stress overshoot, depending on values of $\lambda\dot{\gamma}_0$ and E ; but always increases the N_1 overshoot.

The numerical results for the cessation case are presented in figure 8. Both the shear stress and the first normal stress difference relaxation functions decay monotonically, quickly approaching zero; the curves for $\eta^-/\eta(\dot{\gamma}_0)$ and $\Psi_1^-/\Psi_1(\dot{\gamma}_0)$ overlap. At higher $\lambda\dot{\gamma}_0$ (figure 8, bottom), equilibrium is reached faster than at lower $\lambda\dot{\gamma}_0$ (figure 8, top).

At later times, the material functions decay exponentially. In figure 8, this is seen as regions where the curves become straight lines. The exponential decay is preceded by a region of faster decrease. An analysis of the system (4.32)-(4.35) shows that the eigenvalues of its linearised version corresponding to \mathcal{T}_{12} and \mathcal{D}_1 both equal $-\mathcal{F}(3/b, E/b)$; hence,

$$\frac{\eta^-}{\eta(\dot{\gamma}_0)} \sim \frac{\Psi_1^-}{\Psi_1(\dot{\gamma}_0)} \sim \exp[-\mathcal{F}(3/b, E/b)\bar{t}] \sim \exp(-t/\lambda_e) \quad (4.36)$$

asymptotically at later times, where λ_e is the time constant defined previously by (4.12). Our numerical simulations confirm this result. One should also remark that the whole

relaxation can be effectively approximated by a sum of two exponential decays, where the smaller relaxation time is a non-trivial function of E , b and $\dot{\gamma}_0$, while the larger one, as seen from (4.36), is λ_e .

The impact of E on η^- and Ψ_1^- is two-fold. Firstly, the region of fast decrease at early times, which is abrupt and step-like at large E , becomes smoother and less pronounced, as E decreases (figure 8, right). Secondly, a decrease in E leads to a faster decay rate in the exponential regime at late times, since $\mathcal{F}(3/b, E/b)$ is a decreasing function of E . This effect is seen in figure 8, left.

5. Discussion

5.1. Steady shear flow

The influence of salinity on the non-Newtonian viscosity of polyelectrolytes has been subject to extensive experimental studies. Both a decrease in viscosity and a shift of the onset of shear-thinning towards higher shear rate values with increasing salt concentration are shown by e.g. AitKadi & Carreau (1987), Tam & Tiu (1989, 1990), Stavland *et al.* (2013), and Stanislavskiy (2018). It is also reported that polyelectrolytes the molecules of which are intrinsically more rigid demonstrate shear-thinning in a greater degree. The predictions of the C-FENE-P dumbbell model are in excellent qualitative agreement with these experimental results, as illustrated in figure 1, right.

The predicted value of the shear-thinning exponent, $-2/3$, matches experimental data for dilute partially hydrolysed polyacrylamides (Lozhkina 2018). One should remember, however, that the asymptotic value of $-2/3$ is not always reached in practice. As seen from figure 1, right, the C-FENE-P model can explain experimental values of the shear-thinning exponent in the range between $-2/3$ and 0, which is compatible with the values given by Bird *et al.* (1987a).

Much less data is available on the normal stress coefficients and their dependence on salt concentration. The shape of the $\Psi_1(\dot{\gamma})$ curve predicted by the C-FENE-P model is realistic and fully consistent with a qualitative description given by Bird *et al.* (1987a, §3.3). The simple nonlinear relation between $\Psi_1(\dot{\gamma})$ and $\eta(\dot{\gamma})$, expression (3.9), has been tested experimentally for partially hydrolysed polyacrylamides in a recent study by Lozhkina (2018); this relation was proven to be qualitatively correct for solutions of high-molecular-weight polyacrylamides, but to not hold for their lower-molecular-weight counterparts. The second normal stress difference is reported to be very small, $|\Psi_2(\dot{\gamma})| \ll |\Psi_1(\dot{\gamma})|$; hence, it does not play a significant role for most flows of practical interest (Bird *et al.* 1987a, §3.3). The second normal stress coefficient vanishes in many kinetic theory-based polymer fluid models, see e.g. (Bird *et al.* 1980), including the C-FENE-P dumbbells.

5.2. Steady elongational flow

The C-FENE-P model predicts monotonic elongational thickening at positive elongation rates. The S-shaped curves, obtained in earlier theoretical works of Dunlap & Leal (1984) and Ait-Kadi *et al.* (1988), are not reproduced by our model. The impact of salinity on the elongational viscosity, as described in section 3.2 and shown in figure 2, is in qualitative agreement with available experimental data (Miles *et al.* 1983; AitKadi & Carreau 1987; Dunlap *et al.* 1987; Ferguson *et al.* 1990; Anna *et al.* 1997). For the negative elongation rates, we found no experimental results for comparison.

5.3. Small-amplitude oscillatory shear flow

The qualitative shape and asymptotic behaviour of the complex viscosity components $\eta'(\omega)$, $\eta''(\omega)$ and the elastic moduli $G'(\omega)$, $G''(\omega)$, as described in section 4.1, are in accordance with physical arguments provided by Bird *et al.* (1987a, §3.4). A decrease in these material functions with increasing salinity at fixed ω , shown in figure 5, is supported by experimental observations of Tam & Tiu (1989) and Ihebuzor (2019).

Furthermore, the C-FENE-P model predicts a decrease of the experimental time parameter, λ_e , with increasing salinity, as shown in figure 3; this leads to a shift of the characteristic points, occurring at fixed $\lambda_e\omega$, towards higher frequencies. This matches the experimental results of Ihebuzor (2019), who reported the $G'-G''$ crossover frequency to increase with salinity.

At the same time, the C-FENE-P model is not capable of resolving the quantitative relations between the SAOS material functions; in particular, it predicts that the $G'(\omega)$ and $G''(\omega)$ curves intersect at the point of maximum of $G''(\omega)$, as follows from (4.14). This is not supported by experimental results for polyelectrolytes: as seen from the recent report of Ihebuzor (2019), $G''(\omega)$ continues to increase at frequency values larger than the crossover frequency. This mismatch was expected, since dumbbell models, with their single relaxation time, cannot properly represent a complex oscillator possessing a wide spectrum of relaxation times – which a real polymer molecule is – in cases when the flow pattern changes rapidly. An extension of the C-FENE-P dumbbell model to its bead-spring-chain variant might resolve this issue, but would lead to significant mathematical and computational complexity, which we are intentionally trying to avoid in this work.

Finally, we did not find any experimental works allowing to analyse the results related to the behaviour of the first normal stress difference in SAOS flow.

5.4. Start-up and cessation of steady shear flow

At fixed salinity, the appearance of shear stress overshoot at the start-up of steady shear flow and the way its magnitude and position depends on the step-rate value $\dot{\gamma}_0$, as described in section 4.2 and shown in figure 7, is in excellent qualitative agreement with experiments of Zebrowski & Fuller (1985) and Islam (2019).

According to our results, a decrease in salinity can either increase or decrease the relative shear stress overshoot magnitude, depending on the polyelectrolyte natural rigidity and the step-rate value $\dot{\gamma}_0$. Interestingly, the same complex effect was predicted by advanced numerical study of Andrews *et al.* (1998), who used a polymer model more advanced than ours both mechanically (bead-spring-chains in place of dumbbells) and physically (Debye-Hückel potential instead of simple Coulomb force). Experimentally, this effect was recently observed by Åsen (2019) for aqueous solution of partially hydrolysed polyacrylamide. In earlier experiments, in particular those of Zebrowski & Fuller (1985), it was reported that the relative overshoot increases with decreasing salinity, which is also consistent with our results.

In the case of steady shear flow cessation, the C-FENE-P model predicts a faster return to equilibrium at increasing shear rate values and fixed salinity, as seen in figure 8. This is confirmed by experimental evidence provided by Zebrowski & Fuller (1985) and Islam (2019). Furthermore, our results show that at fixed shear rate value, an increase in salinity leads to a slower decay of shear stresses; this is also in agreement with the results of Zebrowski & Fuller (1985).

Finally, Islam (2019) investigated the shape of normalised shear stress relaxation functions for commercial partially hydrolysed polyacrylamides. Two clearly distinct regions – an exponential decay at later times preceded by a faster decrease at earlier times,

as predicted by the C-FENE-P model – were observed. Furthermore, the decay rate in the exponential regime was found to be dictated by the polymer type and independent of $\dot{\gamma}_0$ and polymer concentration, which is in agreement with our theoretical result expressed by (4.36).

No experimental data for comparison was found for the first normal stress difference growth and relaxation functions.

6. Conclusions

The predictions of the C-FENE-P dumbbell model in steady and transient shear and elongational flows are in a very good qualitative agreement with most of the available experimental data for polyelectrolytes. This involves not only the qualitative shape of the material functions and their dependence on flow parameters, but also the way how the material functions differ for more and less intrinsically rigid polyelectrolytes and how they are affected by the solvent salinity. Furthermore, our results are fully consistent with numerical simulations of the advanced polyelectrolyte model investigated by Andrews *et al.* (1998). At the same time, the C-FENE-P model is strikingly simple, being in fact just slightly more mathematically complicated, compared to the uncharged FENE-P dumbbell model. The closed-form constitutive equation allows to investigate fluid dynamics in shear and shearfree flows using a combination of analytical and simple numerical methods. In addition, physical quantities of interest – such as the relative elongation of the polyelectrolyte molecules – can be easily kept track of under analysis.

Concerning numerical simulation of complex flows, we assume that any computer code which is capable of solving the equations of motion for a FENE-P dumbbell fluid can be easily upgraded to tackle the constitutive equation of the C-FENE-P dumbbells.

We believe that the C-FENE-P dumbbell model has all the potential to be a robust instrument, suitable for direct use in technological applications and allowing a qualitative understanding of flow phenomena in complex flows of dilute polyelectrolyte solutions.

This research has been funded by Norwegian Academy of Science and Letters through VISTA project 6370. Also, the authors acknowledge the Research Council of Norway and the industry partners (2019) of the National IOR Centre of Norway: ConocoPhillips Skandinavia AS, Aker BP ASA, Vår Energi AS, Equinor ASA, Neptune Energy Norge AS, Lundin Norway AS, Halliburton AS, Schlumberger Norge AS, Wintershall Norge AS, and DEA Norge AS – for support. The authors would like to thank the referees for useful remarks. Finally, DS thanks Tamara Shogina for numerous suggestions on text improvements.

REFERENCES

- AIT-KADI, A., GRMELA, M. & CARREAU, P. J. 1988 A rheological equation of state for dilute polymer solutions with applications to polyelectrolytes. *Rheol. Acta* **27**, 241–254.
- AITKADI, A. & CARREAU, P. J. 1987 Rheological properties of partially hydrolyzed polyacrylamide solutions. *J. Rheol.* **31**, 537–562.
- ANDREWS, N. C., MCHUGH, A. J. & SCHIEBER, J. D. 1998 Polyelectrolytes in shear and extensional flows: Conformation and rheology. *J. Polym. Sci. B* **36**, 1401–1417.
- ANNA, S. L., SPIEGELBERG, S. H. & MCKINLEY, G. H. 1997 The transient extensional rheology of polystyrene and polyacrylamide Boger fluids and the effects of salt concentration on the extensibility of PAA macromolecules. In *68th Annual Society of Rheology Meeting*. Galveston, TX.

- ARMSTRONG, R. C. 1974a Kinetic theory and rheology of dilute solutions of flexible macromolecules. I. Steady state behavior. *J. Chem. Phys.* **60**, 729–733.
- ARMSTRONG, R. C. 1974b Kinetic theory and rheology of dilute solutions of flexible macromolecules. II. Linear viscoelasticity. *J. Chem. Phys.* **60**, 724–728.
- ÅSEN, S. M. 2019 Flow behaviour and rheological properties of visco-elastic and ridged (viscous) polymer solutions in brines of different salinities. In *IOR Norway 2019*.
- BIRD, R. B., ARMSTRONG, R. C. & HASSAGER, O. 1987a *Dynamics of Polymeric Liquids. Vol. 1. Fluid Mechanics*. Hoboken, NJ: John Wiley & Sons, Inc.
- BIRD, R. B., CURTISS, C. F., ARMSTRONG, R. C. & HASSAGER, O. 1987b *Dynamics of Polymeric Liquids. Vol. 2. Kinetic Theory*. Hoboken, NJ: John Wiley & Sons, Inc.
- BIRD, R. B., DOTSON, P. J. & JOHNSON, N. L. 1980 Polymer solution rheology based on a finitely extensible bead-spring-chain model. *J. Non-Newtonian Fluid Mech.* **7**, 213–235.
- BIRD, R. B., JR, H. R. WARNER & EVANS, D. C. 1971 Kinetic theory and rheology of dumbbell suspensions with Brownian motion. *Adv. Polym. Sci.* **8**, 1–90.
- DE GENNES, P. G., PINCUS, P., VELASCO, R. M. & BROCHARD, F. 1976 Remarks on polyelectrolyte conformation. *Le Journal de Physique* **37** (12), 1461–1473.
- DUNLAP, P. N. & LEAL, L. G. 1984 The charged dumbbell model for dilute polyelectrolyte solutions in strong flows. *Rheol. Acta* **23**, 238–249.
- DUNLAP, P. N., WANG, C.H. & LEAL, L. G. 1987 An experimental study of dilute polyelectrolyte solutions in strong flows. *J. Pol. Sci. B* **25**, 2211–2238.
- FERGUSON, J., WAITERS, K. & WOLFF, C. 1990 Shear and extensional flow of polyacrylamide solutions. *Rheol. Acta* **29**, 571–579.
- FERRY, J. D. 1980 *Viscoelastic Properties of Polymers*. New York: Wiley.
- GIESEKUS, H. 1962 Elasto-viskose Flüssigkeiten, für die in stationären Schichtströmungen sämtliche Normalspannungskomponenten verschieden groß sind. *Rheol. Acta* **2**, 50–62.
- IHEBUZOR, N. N. 2019 The impact of brine salinity and concentration on small amplitude oscillatory shear (SAOS) flow material functions of EOR polymers. Master's thesis, University of Stavanger, Norway.
- ISLAM, H. 2019 Experimental investigation of material functions of EOR polymer solutions. Master's thesis, University of Stavanger, Norway.
- JIANG, L. & CHEN, S. B. 2001 Electroviscous effect on the rheology of a dilute solution of flexible polyelectrolytes in extensional flow. *J. Non-Newtonian Fluid Mech.* **96**, 445–458.
- KING, M. & EISENBERG, A. 1972 Dilute solution viscoelasticity of simple ionic polymers – A theory for charged beadspring models. *J. Chem. Phys.* (57), 482.
- KRAMERS, H. A. 1944 Het gedrag van macromoleculen in een stroomende vloeistof. *Physica* **11**, 1–19.
- LA NAVE, F. & MAZUR, B. 2002 Reading Bombelli. *The Mathematical Intelligencer* **24**, 12–21.
- LAKE, L. W. 1989 *Enhanced Oil Recovery*. Englewood Cliffs, NJ: Prentice Hall Inc.
- LOZHKINA, A. 2018 Understanding shear flow material functions of EOR polymers. Master's thesis, University of Stavanger, Norway.
- MAITZ, M. F. 2015 Applications of synthetic polymers in clinical medicine. *Biosurface and Biotribology* **1**, 161–176.
- MEZGER, T. G. 2014 *The Rheology Handbook, 4th ed.* Hannover, Germany: Vincentz Network GmbH.
- MILES, M. J., TANAKA, K. & KELLER, A. 1983 The behaviour of polyelectrolyte solutions in elongational flow; the determination of conformational relaxation times (with an Appendix of an anomalous adsorption effect). *Polymer* **24**, 1081–1088.
- OLDROYD, J. G. 1950 On the formulation of rheological equations of state. *Proc. Roy. Soc. A* **200**, 523–541.
- PETERLIN, A. 1966 Hydrodynamics of macromolecules in a velocity field with longitudinal gradient. *J. Polymer Sci. B: Polymer Letters* **4** (4), 287–291.
- SHOGIN, D., AMUNDSEN, P. A., HIORTH, A. & MADLAND, M. V. 2017 Rheology of polymeric flows in circular pipes, slits and capillary bundles: analytical solutions from kinetic theory. In *IOR Norway 2017*.
- SPAGNOLIE, S. E., ed. 2014 *Complex Fluids in Biological Systems: Experiment, Theory, and Computation*. Berlin: Springer.

- STANISLAVSKIY, V. 2018 Investigating the impact of solvent salinity on the viscometric functions of EOR polymers. Master's thesis, University of Stavanger, Norway.
- STAVLAND, A., JONSBRÅTEN, H. & STRAND, D. 2013 When will polymer viscosity be a design criterion for EOR polymer flooding? In *IEA-EOR 34th Annual Symposium*. Stavanger, Norway.
- TAM, K. C. & TIU, C. 1989 Steady and dynamic shear properties of aqueous polymer solutions. *J. Rheol.* **33**, 257–280.
- TAM, K. C. & TIU, C. 1990 Role of ionic species and valency on the steady shear behavior of partially hydrolyzed polyacrylamide solutions. *Colloid Polym. Sci.* **268**, 911–920.
- WARNER, JR, H. R. 1972 Kinetic theory and rheology of dilute suspensions of finitely extendible dumbbells. *Ind. Eng. Chem. Fundamentals* **11**, 379–387.
- WEVER, D. A. Z., PICCHIONI, F. & BROEKHUIS, A. A. 2011 Polymers for enhanced oil recovery: A paradigm for structure-property relationship in aqueous solution. *Progress in Polymer Science* **36**, 1558–1628.
- ZEBROWSKI, B. E. & FULLER, G. G. 1985 Rheo-optical studies of polyelectrolyte solutions in simple shear flow. *J. Rheol.* **29**, 943–954.
- ZHOU, T. & CHEN, S. B. 2006 Computer simulations of diffusion and dynamics of short-chain polyelectrolytes. *J. Chem. Phys.* **124**, 034904–0349012.